
Temporal Contrast Degradation at the Focus of Ultrafast Pulses from High-Frequency Spectral Phase Modulation

Introduction

Ultrafast laser systems generate intensities at focus as high as 10^{22} W/cm² for a variety of relativistic and high-energy-density physics applications. Although several types of amplifiers are used, all systems use chirped-pulse amplification (CPA) to overcome limits caused by optical damage and nonlinearities.¹ CPA uses stretchers and compressors to modify the pulse's spectral phase, increasing its length and lowering the peak power within the amplifier chain. Stretchers and compressors typically rely on diffraction gratings to geometrically disperse the pulse into spectral components.² Imperfections at optical surfaces where the pulse is dispersed imprint directly onto the spectral phase. The group delay of a spectral component equals the derivative of its phase, and therefore high-frequency phase noise scatters energy before and after the main pulse.^{3–6} (This effect is directly analogous to the halo formed around the far field of a lens by high-frequency wavefront noise in the near field.⁷) Any portion scattered before the peak of the pulse that exceeds 10^{11} W/cm² is capable of ionizing solid targets. Therefore, care is needed when selecting stretchers and compressors to ensure they do not degrade the temporal contrast of the laser system, defined as the ratio of the peak of the pulse to the low-intensity pedestal.

This article presents a theoretical analysis of the impact of high-frequency spectral phase modulation on the temporal contrast of ultrafast pulses. A three-dimensional (3-D) treatment is used to extend the results of Ref. 8. The temporal contrast is evaluated in the focal plane, the target location for ultra-intense experiments. The spectral phase imprint in the near field of a spectrally dispersed beam produces space–time coupling in the far field or focal plane. The pedestal is swept across an area in the focal plane many times the size of the diffraction-limited spot. These phenomena raise questions about the validity of applying measurements made in the near field (the usual domain for high-dynamic-range cross-correlators) to the target plane.

A general model is used in the next section to propagate a spectrally dispersed beam through a noisy phase screen.

Expressions are derived for the average intensity of an ultrafast pulse in the near and far fields. In subsequent sections, closed-form results are obtained for Gaussian functional forms that show the impact on temporal contrast of the scale of optical surface modulation, the beam size, and the scale of geometric dispersion in the near field. Analytic results are compared to numeric simulations, and the numeric analysis is extended to include the usual Lorentzian functional form of the power spectral density of optical surfaces. Simulation results are presented for generic stretchers and compressors that show fundamentally different properties of the temporal contrast at the focal plane.

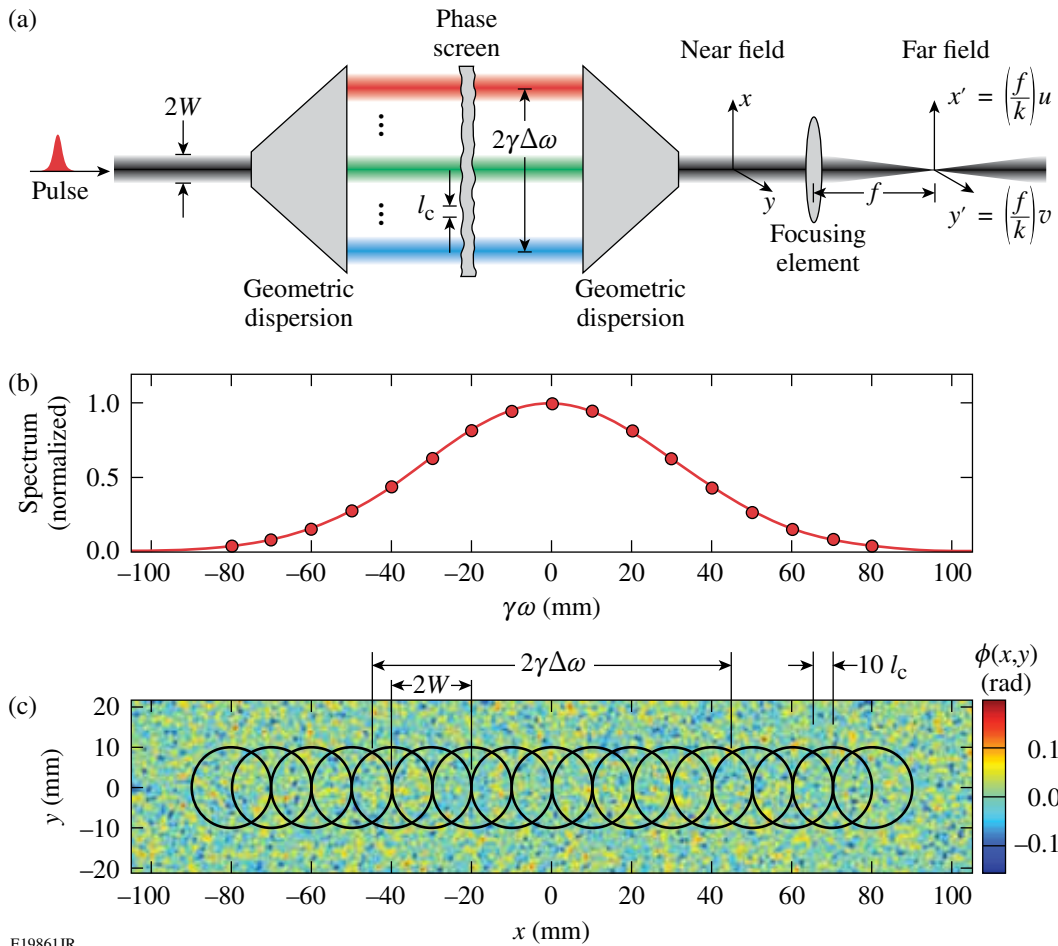
General Expressions for the Temporal Contrast in Near and Far Fields

1. Model

A general schematic of an optical device for spectral phase modification is shown in Fig. 127.9(a). A beam of optical pulses passes through a subsystem that spreads the spectral components using geometric dispersion. The phase of each spectral component is modified using phase screens or other optical systems before a second dispersive component is used to recombine them. Optical pulse stretchers and compressors are examples of this type of device. They modify the chirp of ultrafast pulses by adding or subtracting large, predominantly quadratic spectral phases. High-frequency imperfections in the surface quality of their optics produce unwanted phase modulation. In this article, such imperfections are modeled by adding noisy phase screens to otherwise ideal systems.

A focusing element located in the near field focuses the beam in the far-field plane. The near-field spatial coordinates are (x,y) . The far-field wave-vector components (u,v) are related to the spatial coordinates (x',y') by the focal length f and wave number $k = 2\pi/\lambda$ according to $u = kx'/f$. Figure 127.9(b) shows a Gaussian spectrum spread across the near field. The mapping of spectral components onto the x axis is assumed to be linear. The center of the beam x_0 and a given optical frequency ω are related by

$$x_0(\omega) = \gamma\omega, \quad (1)$$



E19861JR

Figure 127.9

(a) Generic schematic of a system that imprints spectral phase noise on an optical pulse propagating with a finite beam size. The near-field spatial coordinates are (x, y) and the far-field wave-vector components are (u, v) . Three important scale lengths are (1) $\gamma\Delta\omega$, the spatial width of the dispersed spectrum; (2) W , the beam size; and (3) l_c , the correlation length of the phase noise. (b) Gaussian spectrum plotted against the near-field coordinate x ; $\gamma = 0.44$ mm/THz and $\Delta\omega = 100$ THz, corresponding to a 17-fs pulse width. (c) Simulated phase screen $\phi(x, y)$ and beam locations for optical frequencies marked in (b). Scale lengths are $W = 10$ mm, $l_c = 0.5$ mm, and $\gamma\Delta\omega = 44$ mm.

where γ is the spatio-spectral coefficient. The optical frequency ω is defined as the offset from a central frequency ω_0 , which was arbitrarily chosen to correspond to a central wavelength of 910 nm throughout this article.

Figure 127.9(c) shows a simulated realization of a random phase screen, $\phi(x, y)$. The circles denote the beam locations for the spectral components marked on Fig. 127.9(b). Three scale lengths are shown that are key to understanding the impact of phase noise on temporal contrast:

- $\gamma\Delta\omega$ – the optical bandwidth ($1/e$ half-width), scaled onto the near-field axis
- W – the beam size ($1/e$ intensity half-width)
- l_c – the correlation length of the phase noise

Here, l_c can be defined in terms of the correlation function

$$C(x, x', y, y') = \langle \phi(x, y) \phi^*(x', y') \rangle. \quad (2)$$

For a homogeneous, isotropic Gaussian phase screen, the correlation function is related to the correlation length by

$$C(\Delta x, \Delta y) = \sigma^2 \exp\left(-\frac{\Delta x^2 + \Delta y^2}{2l_c^2}\right), \quad (3)$$

where $\Delta x = x - x'$, $\Delta y = y - y'$, and σ is the rms (root mean square) phase of the screen in radians. Depending on the design of the device, the three scale lengths may differ by an order of magnitude or more.

2. Average Far-Field Intensity

In the spectral domain, the optical field of the pulse in the near field is given by

$$\tilde{E}(x, y, \omega) = \tilde{E}_0(x, y, \omega) e^{i\Phi(x, y, \omega)}, \quad (4)$$

where $\tilde{E}_0(x, y, \omega)$ is the input pulse. The spatio-spectral phase function $\Phi(x, y, \omega)$ is related to the phase screen using Eq. (1):

$$\Phi(x, y, \omega) = \phi(x - x_0, y) = \phi(x - \gamma\omega, y). \quad (5)$$

In the limit of small phase modulation ($\phi \ll 1$), the exponential in Eq. (4) is approximated to give

$$\tilde{E}(x, y, \omega) = \tilde{E}_0(x, y, \omega) [1 + i\phi(x - \gamma\omega, y)]. \quad (6)$$

The optical field in the time domain is obtained by a Fourier transform:

$$\begin{aligned} E(x, y, t) &= \int_{-\infty}^{\infty} d\omega \tilde{E}(x, y, \omega) e^{-i\omega t} \\ &= E_0(x, y, t) \\ &\quad + i \int_{-\infty}^{\infty} d\omega \tilde{E}_0(x, y, \omega) \phi(x - \gamma\omega, y) e^{-i\omega t}. \end{aligned} \quad (7)$$

In the far field of a focusing element, the optical field can be expressed in terms of wave-vector components (u, v) , as denoted in Fig. 127.9(a). The double Fourier transform of Eq. (7) gives

$$\begin{aligned} \check{E}(u, v, t) &= \int_{-\infty}^{\infty} \int_{-\infty}^{\infty} dx dy E(x, y, t) e^{-iux} e^{-ivy}, \\ &= \check{E}_0(u, v, t) + i \int_{-\infty}^{\infty} \int_{-\infty}^{\infty} \int_{-\infty}^{\infty} d\omega dx dy \\ &\quad \times \tilde{E}_0(x, y, \omega) \phi(x - \gamma\omega, y) e^{-i(\omega t + ux + vy)}. \end{aligned} \quad (8)$$

The intensity in the far field is $I(u, v, t) = |\check{E}(u, v, t)|^2$. Averaging over an ensemble of phase screens for which $\langle \phi(x, y) \rangle = 0$, the average intensity in the far field is

$$\begin{aligned} \langle I(u, v, t) \rangle &= I_0(u, v, t) + \int_{-\infty}^{\infty} \dots \int_{-\infty}^{\infty} d\omega d\omega' dx dx' dy dy' \\ &\quad \times \tilde{E}_0(x, y, \omega) \tilde{E}_0^*(x', y', \omega') \\ &\quad \times \langle \phi(x - \gamma\omega, y) \phi^*(x' - \gamma\omega', y') \rangle \\ &\quad \times e^{-i(\omega - \omega')t} e^{-i(x - x')u} e^{-i(y - y')v}. \end{aligned} \quad (9)$$

Using a coordinate transformation and completing four integrals [see **Appendix A** (p. 128)], the average far-field intensity can be written in terms of the power spectral density (PSD) of the phase screen:

$$\begin{aligned} \langle I(u, v, t) \rangle &= I_0(u, v, t) \\ &\quad + \int_{-\infty}^{\infty} \int_{-\infty}^{\infty} du' dv' I_0(u', v', t' + \gamma u - \gamma u') \\ &\quad \times \text{PSD}(u - u', v - v'). \end{aligned} \quad (10)$$

Equation (10) is an integral expression for the average far-field intensity given the PSD of the phase screens and I_0 , the far-field intensity without a phase screen. Further analysis is only possible if one assumes functional forms for the integrand.

3. Average Near-Field Intensity

An expression for the average intensity in the near field can be derived using a similar formalism. One starts with an expression similar to Eq. (9), but with all quantities defined in the near field, thereby eliminating the four integrals over the near-field coordinates:

$$\begin{aligned} \langle I(x, y, t) \rangle &= I_0(x, y, t) \\ &\quad + \int_{-\infty}^{\infty} \int_{-\infty}^{\infty} d\omega d\omega' \tilde{E}_0(x, y, \omega) \tilde{E}_0^*(x, y, \omega') \\ &\quad \times \langle \phi(x - \gamma\omega, y) \phi^*(x - \gamma\omega', y) \rangle e^{-i(\omega - \omega')t}. \end{aligned} \quad (11)$$

In this case, it is convenient to use a one-dimensional (1-D) correlation function where the near-field coordinates (x, y) are parameters:

$$C_{xy}(\Delta\omega) = \langle \phi(x - \gamma\omega, y) \phi^*(x - \gamma\omega', y) \rangle. \quad (12)$$

Performing the same coordinate transformation as outlined in **Appendix A** (p. 128), replacing the 1-D correlation function with its Fourier transform PSD_{xy} , and completing integrals of exponentials and a delta function give the following:

$$\langle I(x, y, t) \rangle = I_0(x, y, t) + \int_{-\infty}^{\infty} dt' I_0(x, y, t') \text{PSD}_{xy}(t - t'). \quad (13)$$

That is, the average near-field intensity has an additional term as a result of phase noise that is the convolution of the noise-free intensity and the 1-D power spectral density. This near-field result is similar to that derived in Ref. 8, but without the stated approximations.

The connection between the two-dimensional (2-D) and 1-D PSD functions, $\text{PSD}(u, v)$ and $\text{PSD}_{xy}(t)$, is derived in **Appendix B** (p. 129) and is

$$\text{PSD}_{xy}(t) = \frac{1}{\gamma} \int_{-\infty}^{\infty} dv \text{PSD}(t/\gamma, v). \quad (14)$$

That is, the 1-D temporal PSD is proportional to the integral of the 2-D spatial PSD over one spatial frequency axis after the other axis—the one that defines the plane of geometric dispersion—is replaced by the scaled time axis using $u = t/\gamma$.

Analytic Expressions Assuming Gaussian Functional Forms

It is instructive to consider the case where all quantities are Gaussians. That is, the 2-D PSD function of the phase screen has a Gaussian functional form, as well as the beam profile and the pulse shape. In this case, the integral expressions for the average intensity in the far field [Eq. (10)] and near field [Eq. (13)] can be reduced to closed-form analytic expressions. The PSD is the Fourier transform of Eq. (3):

$$\text{PSD}(u, v) = \frac{\sigma^2 l_c^2}{2\pi} \exp\left[-l_c^2(u^2 + v^2)/2\right]. \quad (15)$$

The noise-free intensity is

$$I_0(u, v, t) = I_P \exp(-\Delta\omega^2 t^2 - W^2 u^2 - W^2 v^2), \quad (16)$$

where I_P is the peak, on-axis intensity at $u = v = t = 0$. The pulse width τ_0 (defined as the half-width at the $1/e$ intensity) is equal to $1/\Delta\omega$. Similarly, the width of the focal spot, w_0 (defined as

the half-width at $1/e$ intensity), is equal to $1/W$. Substitution into Eq. (10) gives

$$\begin{aligned} \langle I(u, v, t) \rangle &= I_0(u, v, t) \\ &+ I_P \frac{\sigma^2 l_c^2}{2W} \left(l_c^2/2 + \gamma^2 \Delta\omega^2 + W^2 \right)^{-1/2} \\ &\times \exp\left[\frac{(\gamma\Delta\omega^2 t - W^2 u)^2}{l_c^2/2 + \gamma^2 \Delta\omega^2 + W^2} \right] \\ &\times \exp\left(-W^2 u^2 - l_c^2 v^2/2 - \Delta\omega^2 t^2 \right). \end{aligned} \quad (17)$$

The second term is the low-intensity pedestal that is produced by the phase screen. The magnitude of the pedestal scales with the variance of the phase, σ^2 . One limit that is often the case for stretchers and small-scale compressors is that the spatial spread of the spectrum across the phase screen ($\gamma\Delta\omega$) is much larger than both the input beam size (W) and the correlation length (l_c). Typical values for the three quantities are of the order of 100 mm, 1 mm, and 100 μm , respectively. Using this limit, the far-field intensity can be approximated as

$$\begin{aligned} \langle I(u, v, t) \rangle &= I_0(u, v, t) + I_P \frac{\sigma^2 l_c}{\sqrt{2} \gamma \Delta\omega} \left(\frac{l_c}{\sqrt{2} W} \right) \\ &\times \exp\left[-W^2 \left(u + \frac{t}{\gamma} \right)^2 - \frac{l_c^2 v^2}{2} - \frac{l_c^2 t^2}{2\gamma^2} \right]. \end{aligned} \quad (18)$$

The expression for the near-field intensity has a similar form, where I_P is the peak intensity in the near field:

$$\langle I(x, y, t) \rangle = I_0(x, y, t) + I_P(x, y) \frac{\sigma^2 l_c}{\sqrt{2} \gamma \Delta\omega} \exp\left(-\frac{l_c^2 t^2}{2\gamma^2} \right). \quad (19)$$

There are several important differences between these two expressions. First, the noise-dependent terms at the peak of the pulse differ by the factor $l_c/\sqrt{2}W$. Typically this factor is much less than unity. Therefore one could expect a much smaller on-axis, noise-dependent contribution in the vicinity of $t = 0$ in the far field than in the near field.

The second and more significant difference is the presence of the space–time coupling term in the exponent: $-W^2(u + t/\gamma)^2$. As a result, the maximum far-field intensity of the pedestal at a given time corresponds to a different transverse location in the far field. The location is determined from the equation

$u = -t/\gamma$. More general results, discussed below, support this conclusion. This space–time coupling is analogous to that reported in certain types of pulse shapers.⁹ In summary, these analytic results, although derived specifically for Gaussian functional forms, show that one should expect large differences between the temporal contrast in the near and far fields.

Comparison of Analytic Results and Numerical Simulations

The analytic expressions were tested against numerical simulations of spatially dispersed ultrafast pulses propagating through phase screens. Table 127.I shows default model parameters, unless explicitly specified. The 2-D PSD function was used to generate a random phase screen of Gaussian random numbers over the entire near-field plane in the dispersed region.¹⁰ An input beam was dispersed into spectral components that were incident on different sections of the phase screen, as shown in Fig. 127.9(c). Beams of each component

were modulated by the screen and then propagated to the far field using 2-D fast Fourier transforms (FFT's). Each spectral component was added coherently. The far-field intensity at each position (u,v,t) was calculated as the magnitude of the total field squared. To avoid noise from interpolation, the near-field and spectral sampling intervals were matched using the spatio-spectral coefficient so that $\delta x = \gamma \delta \omega$.

Figures 127.10–127.12 compare numerical simulations to the analytic results for Gaussian functional forms. The near-field average intensity in the x – t plane is shown in Fig. 127.10(a). The intensity is plotted on a logarithmic scale in dB relative to the peak. The narrow peak down the center around $t = 0$ is the intense, noise-free term $I_0(x,y,t)$ in Eq. (19). The low-intensity pedestal comes from the second, PSD-driven term. In Figs. 127.10(b)–127.10(d) numerical simulations for a single-phase screen realization and the analytic average are compared at three different x positions in the near field. While

Table 127.I: Default simulation parameters used in this article, unless explicitly specified.

Parameter	Symbol	Value	Parameter	Symbol	Value
Center wavelength	λ_0	910 nm	Time step	δt	8 fs
1/e pulse half-width	τ_0	10 fs	Number of time steps	N_T	2^{12}
Near-field beam size	W	1 mm	Near-field step	δx	84 μm
Spatiospectral coefficient	γ	0.44 mm/THz	Number of steps across beam	N_X	2^8
rms phase	σ	0.04 rad	Frequency step	$\delta \omega$	0.19 THz
Correlation length	l_c	100 μm	Phase screen dimensions	$x_{\text{max}}, y_{\text{max}}$	360 \times 21 mm

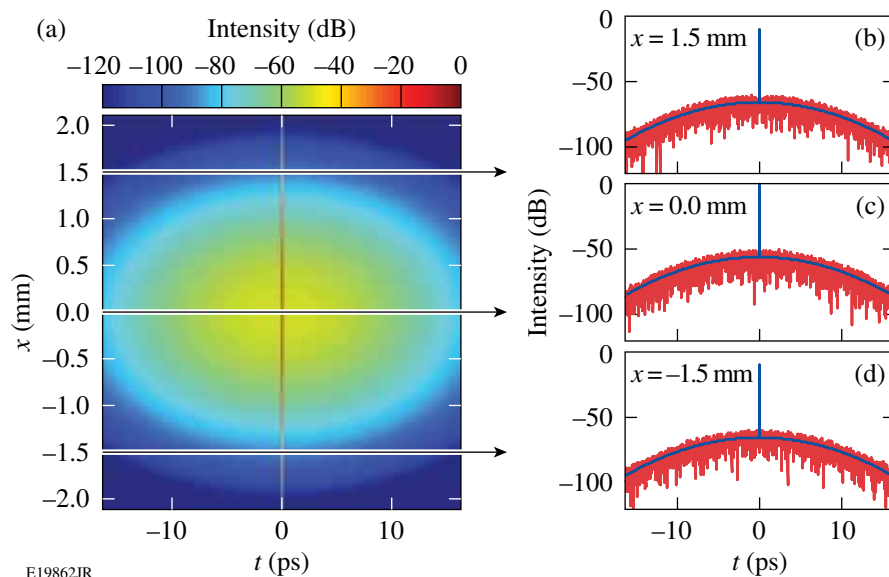


Figure 127.10

(a) Near-field average intensity in the x – t plane calculated using Eq. (19). The main pulse $I_0(x,y,t)$ is the red line at $t = 0$ ps. [(b),(c),(d)] Analytic (blue) and numeric (red) values of intensity calculated at different x values.

E19862JR

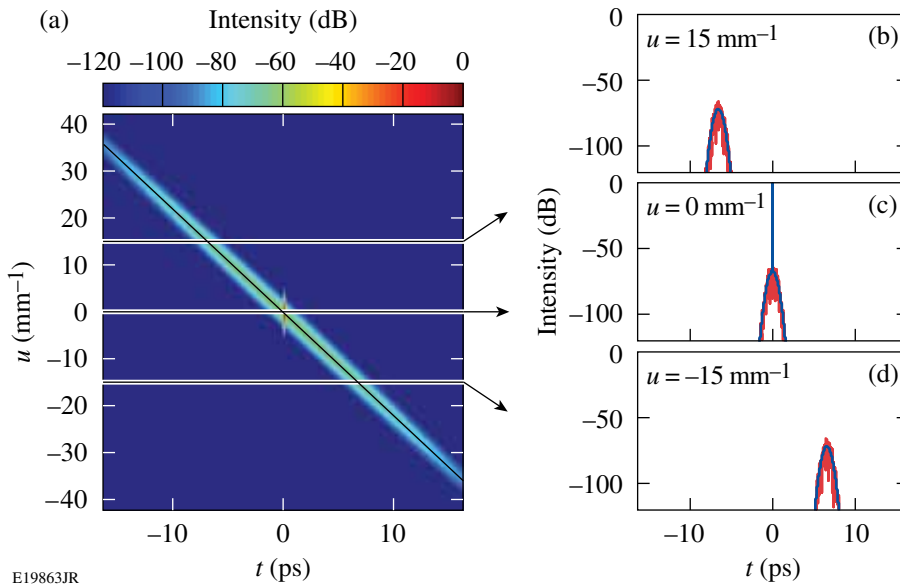


Figure 127.11

(a) Far-field average intensity in the u - t plane calculated using Eq. (18). Space-time coupling in the noise-dependent term follows the black line, $u = -t/\gamma$. [(b),(c),(d)] Analytic (blue) and numeric (red) values of intensity calculated at different u values.

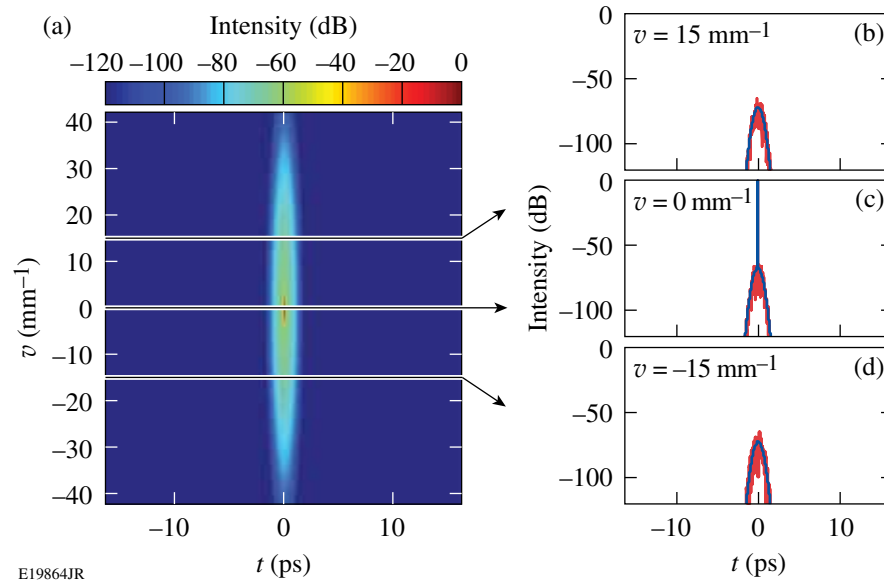


Figure 127.12

(a) Far-field average intensity in the v - t plane calculated using Eq. (17). [(b),(c),(d)] Analytic (blue) and numeric (red) values of intensity calculated at different v values.

the numerical results (red lines) have high-frequency structure, which is a consequence of using a single-phase screen realization, their overall profile follows the analytic results (blue lines).

Results calculated for the far field in the u - t plane, using Eq. (18), are shown in Fig. 127.11. The space-time coupling between u and t appears as a diagonal noise-dependent contribution to the intensity that follows $u = -t/\gamma$. As a consequence, the slices at different u positions show a temporal displacement of the noise-dependent term. In contrast, plots in the v - t plane (Fig. 127.12) do not show space-time coupling. The v axis is conjugate to the y axis, which is orthogonal to the plane of spectral dispersion.

The temporal narrowing on axis in the far field ($u = v = 0$) depends on W , the size of the beam in the near field. Figure 127.13 shows results for four values of W . The far-field intensity approaches the near-field result as the size of the beam is reduced from 3 to 0.1 mm. In this small-beam limit, each spectral component samples only a small portion of the screen, and the statistics become identical to the 1-D case for the near field. The beneficial effect of averaging the phase contributions over multiple correlation lengths no longer occurs, and the on-axis contrast is reduced.

The numeric results have high-frequency structure because they used a single realization of the phase screen. Averag-

ing over multiple pulses (each calculated using a different phase screen) increases the level of agreement between the numeric and analytic results in both the near and far fields (see Fig. 127.14).

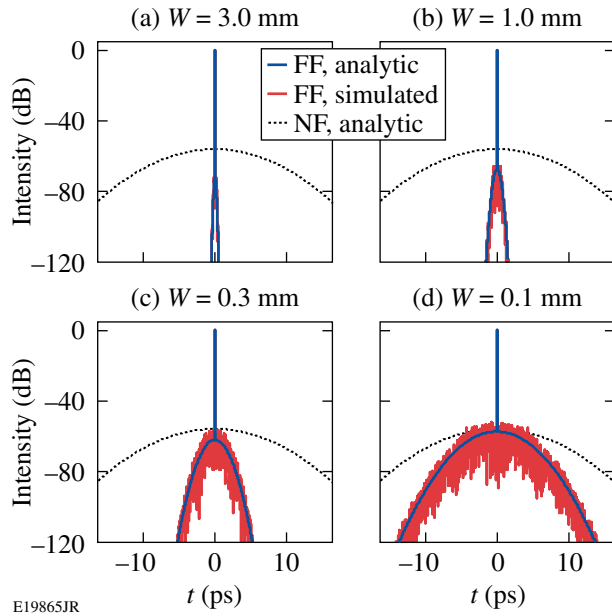


Figure 127.13
On-axis temporal intensities for Gaussian functional forms and a range of near-field beam sizes (W). The on-axis far-field contrast increases with the beam size.

In principle, there can be significant differences between temporal and ensemble averages for non-ergodic phenomena. Since a laser's stretcher or compressor typically uses static optics, an ensemble average over many phase screens is not relevant. Intensity averaging in time may occur, however, depending on the nature of the interaction with a target. The physical processes may not respond quickly enough to follow the high-frequency temporal modulation. In this case, the relevant quantity is the temporal average of the intensity over the response time of the interaction.

Figure 127.15 shows on-axis plots of the intensity in the near field and far field. The red line is a box-car average in time of the temporal intensity from a single realization of the phase screen. The black line is an ensemble average over pulses that were each calculated using an independent realization of the phase screen. The overall profiles are similar; therefore, one can treat intensity noise from phase screens in spectrally dispersed beams as an ergodic process.

The statistical nature of the intensity fluctuations at a given time may be relevant if the target interaction is nonlinear. In

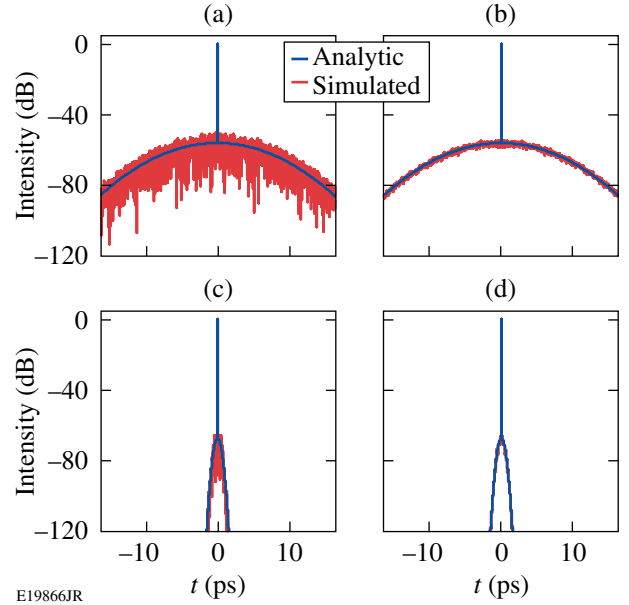


Figure 127.14
On-axis temporal intensities for Gaussian functional forms. Near-field results for (a) one phase screen and (b) an ensemble average of pulses for 25 phase screens. Far-field results for (c) one phase screen and (d) an ensemble average of pulses for 25 phase screens.

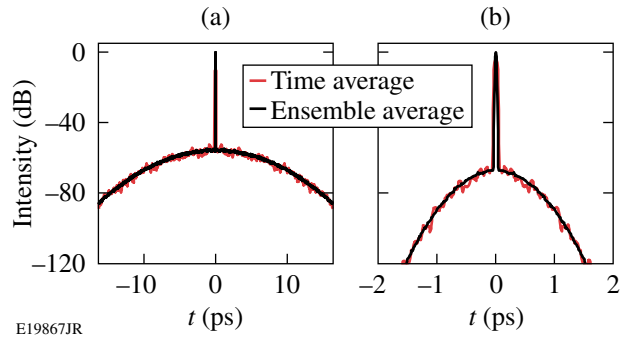


Figure 127.15
Average on-axis intensity calculated either by averaging in time (rectangular window, T) or over an ensemble of phase maps (N). (a) Near-field intensity: $T = 200$ fs, $N = 200$; (b) far-field intensity: $T = 40$ fs, $N = 200$.

general, the intensity-probability distribution for the coherent addition of two beams, one uniform and one statistically fluctuating with a uniform phase distribution $[0, 2\pi]$, is given by¹¹

$$p(I) = \frac{1}{\langle I \rangle} \exp\left(-r - \frac{I}{\langle I \rangle}\right) \mathbf{I}_0\left(2\sqrt{rI/\langle I \rangle}\right), \quad (20)$$

where \mathbf{I}_0 is the modified Bessel function of the first kind of order zero and $r = I_0/\langle I \rangle$. At times where the intensity of the noise-free pulse, I_0 , is much less than that of the pedestal, the parameter $r \ll 1$ and Eq. (19) may be approximated by

$$p(I) \approx \frac{1}{\langle I \rangle} \exp\left(-\frac{I}{\langle I \rangle}\right). \quad (21)$$

Figure 127.16 shows the probability density of the intensity in both the near and far fields at $t = 250$ fs, calculated using an ensemble of phase maps. The numeric results for 200 phase screens are in agreement with the probability calculated using Eq. (21), shown in red.

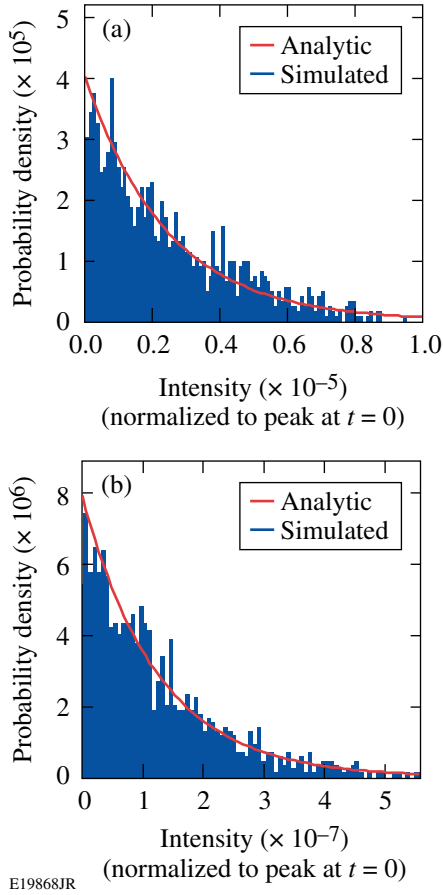


Figure 127.16
Intensity probability distributions at $t = 250$ fs for (a) the near field and (b) the far field.

Lorentzian PSD Functional Forms

Gaussian PSD's are convenient for obtaining closed-form analytic expressions that show the relative impact of the three main scale lengths: $\gamma\Delta\omega$, W , and l_c . In practice, however, optical surfaces do not have Gaussian PSD's. More common are PSD's with a Lorentzian functional form.¹²

$$\text{PSD}(u,v) = \frac{(S-1)\sigma^2 l_c^2}{2\pi(1+l_c^2 u^2 + l_c^2 v^2)^{(S+1)/2}}. \quad (22)$$

The parameter S is the asymptotic slope of the 1-D PSD function. Following Eq. (14), the 1-D PSD in the time domain is

$$\text{PSD}_{xy}(t) = \frac{\sigma^2 l_c \Gamma(S/2)}{\sqrt{\pi} \gamma \Gamma\left(\frac{S-1}{2}\right) \left(1 + l_c^2 t^2 / \gamma^2\right)^{S/2}}, \quad (23)$$

which scales as $1/t^S$ for large times ($t \gg \gamma/l_c$). Typical values of S are in the range of 1.5 to 1.6 (Ref. 12). Despite differences in the functional forms of the Lorentzian and Gaussian PSD's, Fig. 127.17 shows that the nature of the near- and far-field temporal intensities for Lorentzians is qualitatively similar except for a slower fall-off far from the peak.

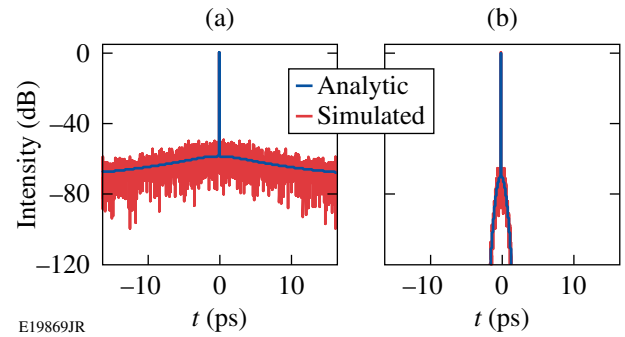


Figure 127.17
On-axis temporal intensity calculated in (a) near field and (b) far field for a Lorentzian PSD with $\sigma = 0.04$ radians, $l_c = 100 \mu\text{m}$, and $S = 1.55$.

Application of Results to Stretchers and Compressors

1. Systems with Multiple Elements

Pulse stretchers and compressors are commonly used in ultrafast CPA laser systems to raise the limits for damage and nonlinearity in their optical amplifiers. Pulses must pass through an even number of dispersing elements such as gratings or prisms to eliminate residual angular dispersion. Additional optical components may be required in portions of the system where the pulse is geometrically dispersed; therefore their surface quality will affect the pulse's temporal contrast. One example is the case of an Öffner stretcher.¹³ Here, two spherical mirrors are used to create an image of a diffraction grating at a "negative" distance from the object, resulting in net positive dispersion for the pulse. It has been shown that the surface quality of stretcher mirrors⁴ and gratings⁶ can have a significant impact on the temporal contrast of the pulse.

It is important, therefore, to be able to apply the preceding results, derived for a single phase screen, to systems with several phase screens. If the phase screens are practically

coincident or imaged onto each other, their phases are summed using the appropriate spatio-spectral coefficients, to get a total phase screen:

$$\Phi_{\text{total}}(x, y, \omega) = \sum_n \phi_n(x - \gamma_n \omega, y). \quad (24)$$

If the phase screens are uncorrelated, the correlation function for the total phase reduces to a sum of correlation functions:

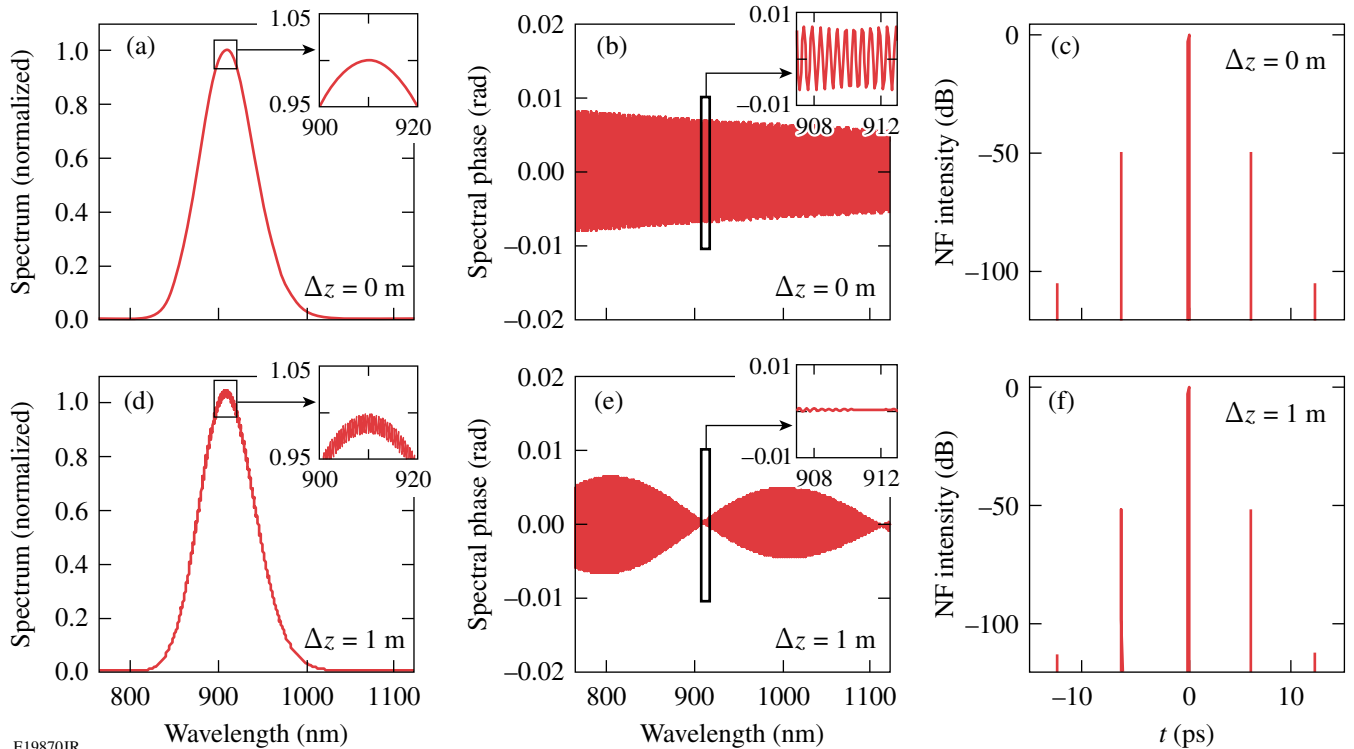
$$\langle \Phi_{\text{total}}(x, y, \omega) \Phi_{\text{total}}^*(x', y', \omega') \rangle = \sum_n C_n(\Delta x - \gamma_n \Delta \omega, \Delta y). \quad (25)$$

In the expressions for the average intensity in the near field or far field, the noise-dependent term becomes a sum over the PSD of each phase screen. For example, in the far field, the average intensity is

$$\begin{aligned} \langle I(u, v, t) \rangle &= I_0(u, v, t) \\ &+ \sum_n \int_{-\infty}^{\infty} \int_{-\infty}^{\infty} du' dv' I_0(u', v', t' + \gamma_n u - \gamma_n u') \\ &\times \text{PSD}_n(u - u', v - v'). \end{aligned} \quad (26)$$

Typically, however, the phase screens are not coincident or imaged onto each other. Significant distances of free propagation (of the order of a meter) are often required to obtain the desired amount of dispersion. In this case, propagation between the surfaces causes high-frequency phase modulation to be converted into amplitude modulation, and vice versa. The distance required for complete phase-to-amplitude conversion is derived from the Talbot effect and is equal to $\Delta x^2/2\lambda$, where Δx is the modulation period.^{14,15} The high-frequency modulation relevant to ultrafast pulse contrast may have periods as short as $100 \mu\text{m}$, for which the phase-to-amplitude conversion distance at $1 \mu\text{m}$ is only 5 mm.

A full description, analytical or numerical, that includes diffraction is complicated. Such an approach, however, is not required when estimating the overall impact on temporal contrast from a series of phase screens. Although near-field propagation changes the fine-scale structure, it has only a minor effect on the average intensity. This is because amplitude modulation degrades the temporal contrast in a way that is very similar to phase modulation. This is shown in Fig. 127.18, where



E19870JR

Figure 127.18

Near-field quantities after spectrally dispersed propagation through a sinusoidal phase screen with a modulation period and amplitude of $450 \mu\text{m}$ and 0.5 nm , respectively. (a) The spectrum, (b) spectral phase, and (c) temporal intensity immediately after the screen. [(d),(e),(f)] The same quantities after propagating a distance of 1 m. There is complete conversion of phase-to-amplitude modulation at the peak wavelength of 910 nm .

the near-field properties of a pulse (spectrum, spectral phase, and temporal intensity) are shown at two distances from a sinusoidal phase screen with a 450- μm period. The simulations show clear evidence of phase-to-amplitude conversion after propagation over 1 m. The resulting satellite pulses, however, are qualitatively similar in magnitude and temporal location.

This conclusion is reinforced in Fig. 127.19, which shows results from numeric simulations that included scalar Fresnel propagation between two Lorentzian phase screens. The distance between them was varied and the far-field intensity in the u - t plane was calculated. In one case, shown in Fig. 127.19(a), the two Lorentzian phase screens were coincident. In Fig. 127.19(b), the screens were separated by 1 m. Differences can be seen in the fine-scale structure, but the average far-field intensity is very similar, even though the separation between phase screens is orders of magnitude more than the coherence length, $l_c = 100 \mu\text{m}$, and the beam size, $W = 1 \text{ mm}$.

For the remainder of this article, therefore, diffraction is not included when estimating the nature of temporal contrast degradation for standard stretcher and compressor designs. Instead, the contributions from each phase screen are added according to Eq. (26).

2. Grating-Based Pulse Compressor and Öffner Stretcher

A schematic of a standard four-grating compressor is shown in Fig. 127.20(a). The gratings, G_1 and G_2 , in the first pair geometrically disperse the input pulse into its spectral components, which are recombined by the second pair. The group delay through the compressor for each component decreases approximately linearly with frequency, corresponding to negative dispersion.^{2,16} The magnitude of dispersion depends on the slant distances between the gratings in each pair, which are usually, but not always, matched.¹⁷ The compressor produces short pulses by compensating for the residual positive dispersion of the stretcher and amplifier glass.

Nonuniformity in the optical surfaces of G_2 and G_3 imprints onto the spectral phase of the pulse. The two gratings can be modeled as perfect elements plus additional phase screens. A retroreflector, placed at the AA' plane to halve the number of required gratings, can potentially degrade the temporal contrast and would be treated as a third phase screen.

A simulation of the output far-field intensity is shown in Fig. 127.20(b). The PSD parameters for the gratings were chosen arbitrarily according to Table 127.I. In this device, the

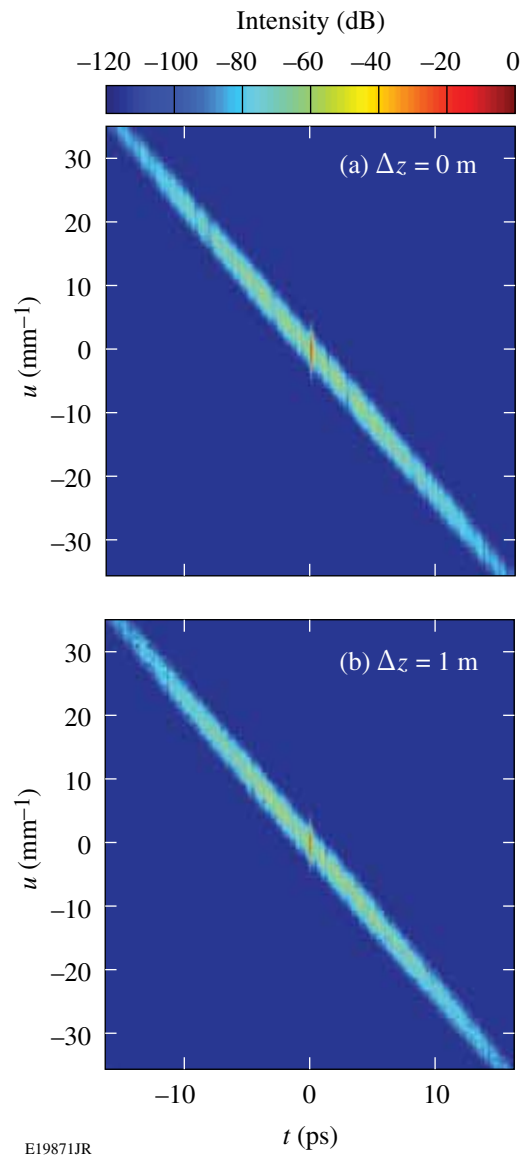
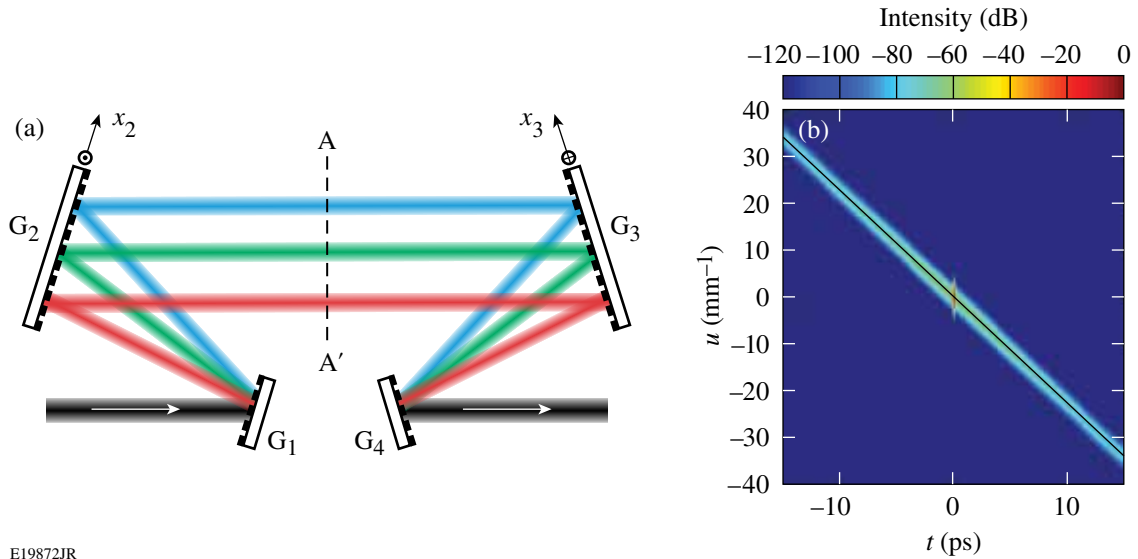


Figure 127.19

Far-field intensity calculated in the u - t plane for two phase screens. (a) Simulation results where phase screens were coincident, and (b) simulation results where phase screens were separated by $\Delta z = 1 \text{ m}$. Each spectral field after the first phase screens was propagated to the second using a scalar Fresnel propagation code. The details of the intensity structure between (a) and (b) are different, but any differences between the average profiles are insignificant.

two phase screens have the same spatio-spectral coefficient, $y = 0.44 \text{ mm/THz}$, and therefore the noise contributions from each grating follow the same line $u = -t/\gamma$.

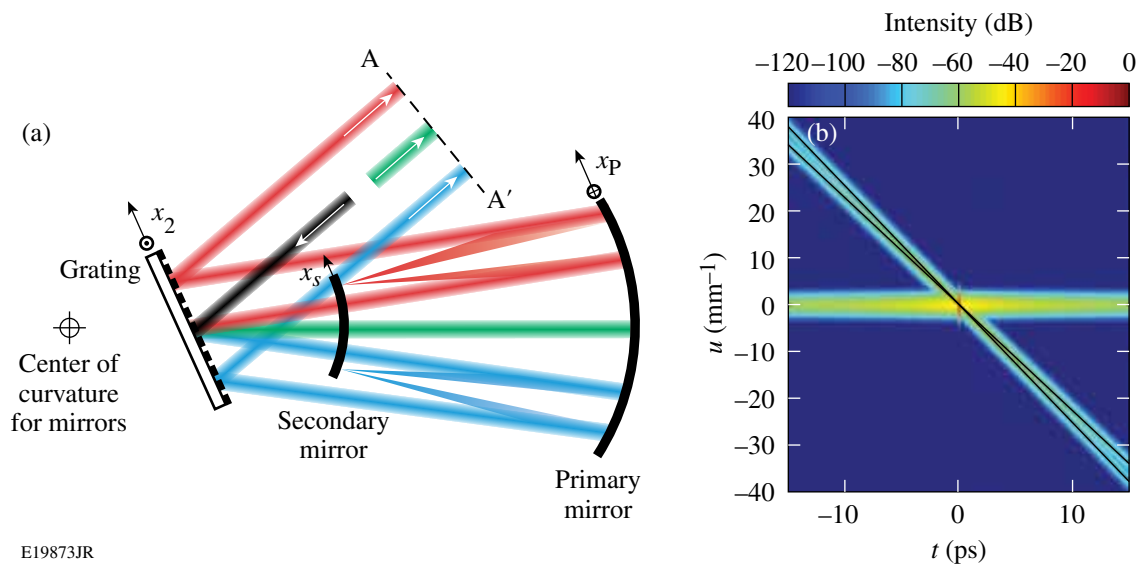
The far-field intensity distribution for an Öffner stretcher is qualitatively different (see Fig. 127.21). In this device, positive dispersion is obtained using a primary and secondary mir-



E19872JR

Figure 127.20

(a) Schematic of a four-grating compressor, showing the input and output beams (black) and three spectral components. Modulation on the surfaces of G_2 and G_3 produces spectral phase noise. A roof mirror can be used along the line AA' to retroreflect the beam, halving the required number of gratings. (b) Far-field average intensity calculated using Lorentzian PSD's in the $u-t$ plane at $t = 0$. G_2 and G_3 have the same spatio-spectral coefficient, $\gamma = 0.44$ mm/THz. The black line corresponds to $u = -t/\gamma$ and tracks the peak intensity from the PSD term.



E19873JR

Figure 127.21

(a) Schematic of an Öffner stretcher, showing the input beam (black) and three spectral components. (b) Far-field average intensity calculated using the same Lorentzian PSD for each optic in the $u-t$ plane at $t = 0$.

ror to form an image of a single grating, thereby achieving a negative separation distance.¹³ Modulation on the surfaces of the grating and primary and secondary mirrors produces spectral phase noise. A roof mirror (not shown) is typically used along the line AA' to retroreflect the beam at a different height back through the stretcher, eliminating spatial chirp. In

this simulation, the spatio-spectral coefficients γ are 0.44, 0.22, and 0.40 mm/THz for the primary mirror, secondary mirror, and grating, respectively.

The secondary mirror is located at a focal plane for each spectral component so, therefore, phase noise added to each

component is transferred directly to the system's far field. The resulting pedestal is centered on the main focal spot (at $u = v = 0$) and can be calculated using Eq. (13), but with spatial coordinates (x', y') replaced with angular coordinates (u, v) , where $u = kx/f$. The primary mirror and grating are located in the near-field planes, however, and therefore the pedestals that they produce are swept across the focal spot, as predicted by Eq. (10).

When identical PSD's are assumed for all optics, the secondary mirror has the largest impact on the contrast degradation. This is fundamentally different than on a compressor, where the surface quality of all optics in the spectrally dispersed planes affects the contrast equally.

Conclusions

A theoretical study was presented on the impact of high-frequency spectral phase modulation on the temporal contrast of ultrafast pulses. Expressions were derived for the intensity pedestal produced by optical surface roughness of components within pulse stretchers and compressors. The average intensity in the far field—the target location for ultra-intense experiments—was evaluated. Analytic closed-form expressions show that spectral phase imprint in the near field of a spectrally dispersed beam produces space–time coupling in the far field. As a result, the low-intensity pedestal that precedes the peak of the pulse sweeps across the target, covering an area many times the diffraction-limited spot size. Simulations of standard stretcher and compressor designs show fundamentally different forms of temporal contrast degradation at focus. These observations raise interesting questions about the nature of the target interaction when such impairments are present and about the validity of applying measurements made in the near field (the usual domain for high-dynamic-range cross-correlators¹⁸) to the target plane.

ACKNOWLEDGMENT

This work has been supported by the U.S. Department of Energy Office of Inertial Confinement Fusion under Cooperative Agreement No. DE-FC52-08NA28302, the University of Rochester, and the New York State Energy Research and Development Authority. The support of DOE does not constitute an endorsement by DOE of the views expressed in this article.

Appendix A

Equation (10) is obtained from Eq. (9) by first replacing variable pairs such as x and x' with X and Δx , where $X = x + x'$ and $\Delta x = x - x'$. The Jacobian of each transformation is 1/2. Equation (9) is then written as

$$\begin{aligned} \langle I(u, v, t) \rangle &= I_0(u, v, t) \\ &+ \frac{1}{2^3} \int_{-\infty}^{\infty} \dots \int_{-\infty}^{\infty} d\Omega d\Delta\omega dX d\Delta x dY d\Delta y \\ &\times \tilde{E}_0\left(\frac{X + \Delta x}{2}, \frac{Y + \Delta y}{2}, \frac{\Omega + \Delta\omega}{2}\right) \\ &\times \tilde{E}_0^*\left(\frac{X - \Delta x}{2}, \frac{Y - \Delta y}{2}, \frac{\Omega - \Delta\omega}{2}\right) \\ &\times C(\Delta x - \gamma\Delta\omega, \Delta y) e^{-i\Delta\omega t} e^{-i\Delta x u} e^{-i\Delta y v}, \end{aligned} \quad (27)$$

where the phase map has been assumed to be wide-sense stationary, so that

$$C(\Delta x, \Delta y) = \langle \phi(x, y) \phi^*(x', y') \rangle. \quad (28)$$

The integrals over Ω , X , and Y involve only the spectral near fields \tilde{E}_0 and not the correlation function. Replacing these fields with their temporal Fourier transforms adds integrals over t' and t'' to give a portion of the integrand of Eq. (27) that is

$$\begin{aligned} \int_{-\infty}^{\infty} \dots \int_{-\infty}^{\infty} d\Omega dX dY dt' dt'' E_0\left(\frac{X + \Delta x}{2}, \frac{Y + \Delta y}{2}, t'\right) \\ \times E_0^*\left(\frac{X - \Delta x}{2}, \frac{Y - \Delta y}{2}, t''\right) \\ \times e^{i\left(\frac{\Omega + \Delta\omega}{2}\right)t'} e^{-i\left(\frac{\Omega - \Delta\omega}{2}\right)t''}. \end{aligned} \quad (29)$$

Collecting exponential factors that depend only on Ω and completing the integral gives a Dirac delta function $2\delta(t' - t'')$. This allows one to evaluate the t'' integral, giving

$$\begin{aligned} 2 \int_{-\infty}^{\infty} \dots \int_{-\infty}^{\infty} dX dY dt' E_0\left(\frac{X + \Delta x}{2}, \frac{Y + \Delta y}{2}, t'\right) \\ \times E_0^*\left(\frac{X - \Delta x}{2}, \frac{Y - \Delta y}{2}, t'\right) e^{i\Delta\omega t'}. \end{aligned} \quad (30)$$

That is, each field in Eq. (27) is replaced by its temporal Fourier transform, the integral over Ω is replaced by an integral over its conjugate variable, and a phase factor of $2e^{i\Delta\omega t'}$ is added. Repeating this operation for the integrals over X and Y gives the following equivalent expression for Eq. (29):

$$2^3 \int_{-\infty}^{\infty} \dots \int_{-\infty}^{\infty} dt' du' dv' I_0(u', v', t') e^{i\Delta\omega t'} e^{i\Delta x u'} e^{i\Delta y v'}. \quad (31)$$

Equation (27) is therefore rewritten as

$$\begin{aligned} \langle I(u, v, t) \rangle &= I_0(u, v, t) \\ &+ \int_{-\infty}^{\infty} \dots \int_{-\infty}^{\infty} du' dv' dt' d\Delta\omega d\Delta x d\Delta y I_0(u', v', t') \\ &\times C(\Delta x - \gamma\Delta\omega, \Delta y) \\ &\times e^{-i\Delta\omega(t-t')} e^{-i\Delta x(u-u')} e^{-i\Delta y(v-v')}. \end{aligned} \quad (32)$$

The integrals over Δx and Δy are Fourier transforms of the correlation function, which is equal to the power spectral density of the phase screen and is defined as

$$\text{PSD}(u, v) = \int_{-\infty}^{\infty} d\Delta x d\Delta y C(\Delta x, \Delta y) e^{-i\Delta x u} e^{-i\Delta y v}, \quad (33)$$

The remaining integral over $\Delta\omega$ is evaluated to give the Dirac delta function $\delta(t - t' + \gamma u - \gamma v)$. This makes it possible to complete the integral over t' , which gives

$$\begin{aligned} \langle I(u, v, t) \rangle &= I_0(u, v, t) \\ &+ \int_{-\infty}^{\infty} \int_{-\infty}^{\infty} du' dv' I_0(u', v', t' + \gamma u - \gamma v) \\ &\times \text{PSD}(u - u', v - v'). \end{aligned} \quad (34)$$

Appendix B

Equation (14) is obtained by first integrating the 2-D PSD function over v , the axis normal to the plane of geometric dispersion:

$$\begin{aligned} &\int_{-\infty}^{\infty} \text{PSD}(u, v) dv \\ &= \int_{-\infty}^{\infty} \int_{-\infty}^{\infty} d\Delta x d\Delta y C(\Delta x, \Delta y) e^{-i\Delta x u} \left(\int_{-\infty}^{\infty} dv e^{-i\Delta y v} \right). \end{aligned} \quad (35)$$

The quantity in parentheses is equal to $\delta(\Delta y)$, making it possible for the integral over Δy to complete. Finally, by noting

that $C(-\gamma\Delta\omega, 0) = C_{xy}(\Delta\omega)$, making the substitutions $\Delta x = \gamma\Delta\omega$ and $u = t/\gamma$, and using the fact that

$$\text{PSD}_{xy}(t) = \int_{-\infty}^{\infty} d\Delta\omega C_{xy}(\Delta\omega) e^{-i\Delta\omega t},$$

one obtains the connection between the two PSD functions:

$$\int_{-\infty}^{\infty} dv \text{PSD}(t/\gamma, v) = \gamma \text{PSD}_{xy}(t). \quad (36)$$

REFERENCES

1. P. Maine *et al.*, IEEE J. Quantum Electron. **24**, 398 (1988).
2. E. B. Treacy, IEEE J. Quantum Electron. **QE-5**, 454 (1969).
3. A. Antonetti *et al.*, Appl. Phys. B **65**, 197 (1997).
4. V. Bagnoud and F. Salin, J. Opt. Soc. Am. B **16**, 188 (1999).
5. K.-H. Hong *et al.*, Appl. Phys. B **81**, 447 (2005).
6. C. Hooker *et al.*, Opt. Express **19**, 2193 (2011).
7. J. W. Goodman, *Statistical Optics*, Wiley Series in Pure and Applied Optics (Wiley, New York, 1985).
8. C. Dorrer and J. Bromage, Opt. Express **16**, 3058 (2008).
9. M. M. Wefers and K. A. Nelson, IEEE J. Quantum Electron. **32**, 161 (1996).
10. E. Sidick, in *Modeling Aspects in Optical Metrology II*, edited by H. Bosse, B. Bodermann, and R. M. Silver (SPIE, Bellingham, WA, 2009), Vol. 7390, p. 73900L.
11. J. C. Dainty, J. Opt. Soc. Am. **62**, 595 (1972).
12. E. L. Church, P. Z. Takacs, and T. A. Leonard, in *Scatter from Optical Components*, edited by J. C. Stover (SPIE, Bellingham, WA, 1990), Vol. 1165, pp. 136–150.
13. G. Chériaux *et al.*, Opt. Lett. **21**, 414 (1996).
14. H. F. Talbot, Lond. & Edin. Phil. Mag. & J. of Sci., Third Series **9**, 401 (1836).
15. P. Latimer and R. F. Crouse, Appl. Opt. **31**, 80 (1992).
16. I. Walmsley, L. Waxer, and C. Dorrer, Rev. Sci. Instrum. **72**, 1 (2001).
17. H. Huang and T. J. Kessler, Opt. Lett. **32**, 1854 (2007).
18. S. Luan *et al.*, Meas. Sci. Technol. **4**, 1426 (1993).